OR-94-20-3

A TWO-DIMENSIONAL NUMERICAL MODEL FOR NATURAL CONVECTION IN A VERTICAL, RECTANGULAR WINDOW CAVITY

John L. Wright, Ph.D., P.Eng.
Member ASHRAE

Henry F. Sullivan, Ph.D., P.Eng.
Member ASHRAE

ABSTRACT

It is common for sealed glazing units to exhibit condensation problems when operated in cold climates. Condensation often forms along the perimeter of the exposed surface of the indoor glazing because of the thermal short circuit caused by the edge seal. Furthermore, condensation most readily forms along the bottom edge of the indoor glazing because of the combined effects of edge seal conduction and fill gas convection. A simple two-dimensional numerical control volume formulation is presented that can be used to model the natural convection of gas within a vertical, rectangular cavity. Details of a unique perturbation scheme used to generate secondary cells are also presented. This model closely reproduces the average Nusselt number results of more complex numerical models. Average and local Nusselt numbers have also been compared with experimental results and close agreement has been demonstrated for conditions typical of window cavities.

INTRODUCTION

Most windows manufactured today contain a glazing system that is packaged in the form of a sealed, insulated glazing unit (IGU). The IGU consists of two panes of glass that are separated from each other by an edge seal. The edge seal isolates the space between the glazings, thereby reducing the number of surfaces to be cleaned and creating an insulating cavity suitable for nondurable low-emissivity (low-e) coatings and/or substitute fill gases.

It is widely recognized that the edge seal creates a thermal bridge at the perimeter of the IGU. This is an area of increased thermal stress, high energy loss, and the site of condensation in winter. The remarkable reductions in center-glass heat transfer available through the use of low-e coatings and low-conductivity fill gases accentuate the conductive nature of the edge seal. Until recently, few options were commercially available to increase the thermal resistance of the edge seal. Earlier design improvements dealt mainly with the requirements of the edge seal to exclude moisture, provide a desiccant for the sealed space, and retain the structural integrity of the IGU.

A variety of edge seals with significantly increased thermal resistance have now been designed and marketed, but none offers more thermal resistance than the center-glass portion of an IGU. Consider a double-glazed IGU constructed with a low-e coating and argon fill gas. The thermal resistance of the 1/2-in. (12.7-mm) gap between the glazings is about R-3 (i.e., 3 $h \cdot ft^2 \cdot °F/Btu$ [0.53 $m^2 \cdot °C/W$]). The conductivity of a 1/2-in. layer of material giving the same thermal resistance would be 0.014 $Btu/h \cdot ft \cdot °F$ (0.024 $W/m \cdot °C$), but the conductivities of sealant materials range upward from about 0.14 $Btu/h \cdot ft \cdot °F$ (0.24 $W/m \cdot °C$) and the conductivities of metals are orders of magnitude higher still.

In winter, the flow of fill gas within an IGU cavity contributes to the condensation problem at the bottom edge of the indoor glazing. Fill gas flows upward near the indoor glazing and downward near the outdoor glazing. The descending gas becomes progressively colder. At the bottom of the cavity, this cold fill gas turns and flows close to the bottom of the indoor glazing where it starts its ascent. Thus, the glass near the bottom edge of the indoor glazing is cooled by the coldest fill gas. A similar situation occurs at the top of the cavity, where the fill gas heats the top of the outdoor glazing.

Experimental results support the idea that fill gas motion contributes to the bottom-edge condensation problem. Heat flux measurements using a guarded heater plate apparatus (Wright and Sullivan 1988) have consistently shown that the heat flux to the bottom of the warm-side glazing is higher than the heat flux to the top of the same glazing. Clearly, any model attempting to quantify local heat transfer rates in these regions or attempting to determine the

John L. Wright is a manager and research engineer and **Henry F. Sullivan** is a professor in the Department of Mechanical Engineering, University of Waterloo, Waterloo, ON, Canada.

temperature distribution across the face of the glazing must account for both the edge-seal heat loss and the natural convection of the fill gas.

Recent research has uncovered a great deal of information about the quantification of, and mechanisms governing, heat transfer in edge seals (Wright and Sullivan 1989b; Fraser et al. 1993; Wright et al. 1994). However, none of the methods currently in widespread use for calculating edge-glass heat loss (Frank and Mühlebach 1987; ASHRAE 1993; EE 1989) accounts for fill gas convection. Therefore, they give no information about the differences in heat flux that can be expected between the bottom and top edges of a glazing system. Nor can they be used to determine the minimum indoor pane temperature needed to evaluate the condensation resistance of a window.

Objective

The primary objective of this study was to formulate a two-dimensional numerical model that can be used for the simulation of natural convection in a tall, vertical, rectangular cavity. This model could then be used to simulate heat transfer in glazing systems with sufficient detail to reliably determine the minimum indoor pane temperature and to predict the ability of the window to resist the formation of condensation. Another important objective was to validate the numerical model using experimental results and data from other simulations.

Background

The analysis of heat transfer in the interpane cavity requires treatment of fill gas flow in a tall, vertical, rectangular slot. The fill gas is heated by one wall and cooled by the other. The wall temperatures may not be uniform. Little information has been published about heat transfer in this situation. However, many studies have dealt with the similar and simpler problem of heat transfer in a rectangular cavity where a temperature difference between vertical, isothermal walls drives a convective flow and zero heat flux (ZHF) or where linear temperature profile (LTP) end conditions apply. (The geometry and some definitions are shown in Figure 1.) Useful information exists regarding variables that affect the fill gas flow, the various flow regimes, instabilities in the flow, conditions under which certain flow regimes occur, and details concerning effective modeling. The following paragraphs summarize the most pertinent information available. More detailed reviews have been given by Wright and Sullivan (1989a) and Wright (1990).

The solution is a function of the Rayleigh number (Ra), the aspect ratio of the cavity (A), and the Prandtl number of the fluid (Pr). Few studies have dealt with conditions typical of an IGU: $A \geq 40$, for gases Pr ≈ 0.71, and $Ra < 1.2 \times 10^4$ for optimum pane spacing. The most suitable set of measured heat transfer data is that of ElSherbiny et al. (1982). It is especially useful because it is based on a well-established experimental procedure carried out over wide ranges of Ra and A with the specific aim of independently resolving the roles of Ra and A. The data of ElSherbiny et al. (1982) are shown in Figure 2, where the heat transfer between the walls of the vertical cavity (LTP) is expressed in nondimensional form as the Nusselt number (Nu) versus Ra. Similar sets of Nu versus Ra data have also been generated by Shewen (1986) using a similar apparatus.

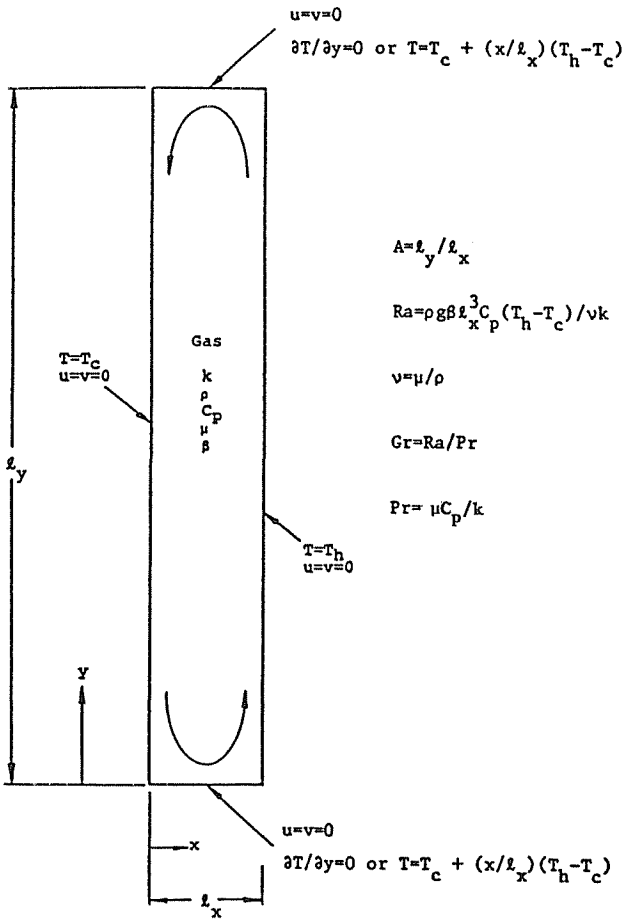

Figure 1 *Problem domain for the analysis of natural convection in a vertical slot.*

When a small temperature difference (i.e., small Ra) is applied across the gas layer, a weak unicellular flow exists, and the temperature profile across the cavity is linear. Heat transfer takes place primarily by conduction, except for small regions at the ends of the cavity, with the result that Nu = 1. When the temperature difference is increased, the flow strengthens and pulls closer to the walls in the form of two increasingly independent boundary layers. More heat transfer takes place by convection via the boundary layers and total heat transfer increases (Nu > 1).

If Ra is increased sufficiently, instabilities occur that create time-dependent flow and eventually a turbulent boundary-layer flow. The transition from laminar to turbulent flow can readily be pinpointed in the approximate method of Raithby et al. (1977) shown in Figure 2. Turbu-

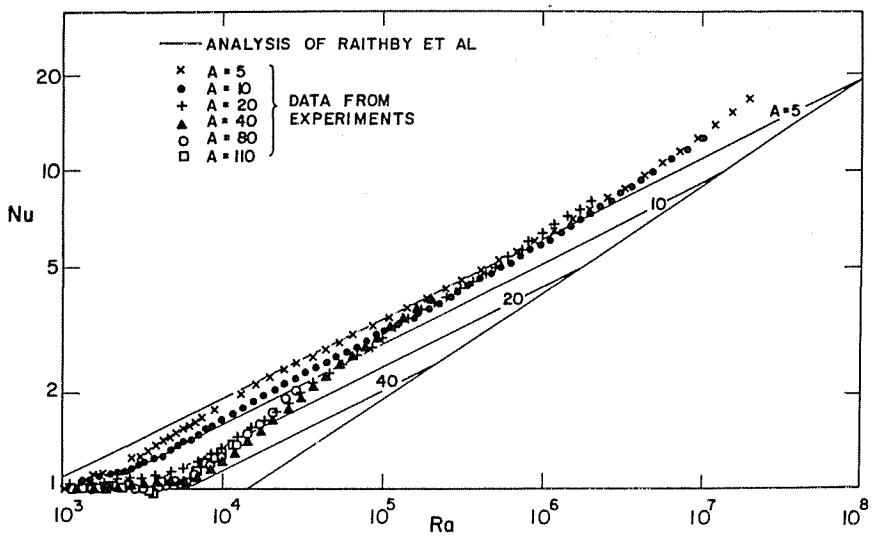

Figure 2 *Nu vs. Ra and* A *data of ElSherbiny et al. (1982) for air in a vertical cavity.*

lent flow is represented by the line that extends upward to the right with a slope of one-third. The lines inside the knee created by the turbulent boundary-layer line and the horizontal axis have a slope of one-fourth and represent laminar boundary-layer flow for various values of A.

It is known that, under some conditions, a steady secondary flow exists. This secondary flow consists of a regular "cat's-eye" pattern of transverse, co-rotating, stationary cells within the core of the base flow.

Many numerical solutions to the equations of motion have been generated for a fluid in a rectangular enclosure, but few address the problem of high aspect ratio. Raithby and Wong (1981) gave finite-difference predictions for heat transfer across vertical air layers with $2 < A < 80$ and $10^3 < \text{Ra} < 3 \times 10^5$. Their results were compared with the experimental results of ElSherbiny et al. (1982). They showed that, for each value of A, the predicted rate of heat transfer closely matched the measured rate of heat transfer up to the critical value of Ra, calculated using the method of Bergholz (1978), at which the onset of secondary flow is expected. At higher values of Ra, the calculated heat transfer rates fell below the measured values. This difference between the measured and predicted results can readily be explained because secondary cells were not predicted by the analysis.

Several numerical models have been able to resolve secondary cells in the vertical slot (Lee and Korpela 1983; Korpela et al. 1982; Ramanan and Korpela 1989; de Vahl Davis and Jones 1984; Lauriat and Desrayaud 1985; Roux et al. 1979). Some authors point out that the onset of secondary instabilities can be delayed by the false diffusion resulting from numerical upwinding schemes. Each model capable of generating cells included special provisions to accurately calculate the convection terms in the flow. Most models were based on high-order discretization schemes (Lee and Korpela 1983; Ramanan and Korpela 1989; Roux et al. 1979; Chait and Korpela 1989). Others claimed to have avoided false diffusion by using a central difference discretization scheme and uniform grids (de Vahl Davis and Jones 1984; Lauriat and Desrayaud 1985).

Noteworthy results were produced by Lee and Korpela (1983), who modeled laminar airflow in a vertical slot for $3.5 \times 10^3 < \text{Ra} < 1.75 \times 10^5$. The results of this simulation included the onset of secondary cells at Ra_c between 7×10^3 and 7.7×10^3 with $A = 20$. They pointed out that cells are not expected to develop for $A < 12$. Lee and Korpela (1983) also compared their predicted values of Nu with the experimental results of ElSherbiny et al. (1982). In this case, the predicted heat transfer rates were in close agreement with the measured heat transfer rates to appreciably higher values of Ra than was the case with the predictions of Raithby and Wong (1981). For instance, at $A = 40$ and $\text{Ra} = 2 \times 10^4$, the predictions of Lee and Korpela agree with the experiment to within 10%, while the predictions of Raithby and Wong show a discrepancy of 10% by $\text{Ra} \approx 1.2 \times 10^4$. The improved agreement with measurement was attributed directly to their ability to resolve the secondary cells. The results of Lee and Korpela consistently underpredict the measured values of Nu at higher values of Ra ($\text{Ra} > 1.2 \times 10^4$ for $A = 40$).

Korpela et al. (1982) showed that the results of Bergholz (1978) could be simplified to predict the critical value of the Grashof number ($\text{Gr} = \text{Ra}/\text{Pr}$), Gr_c, at which the onset of secondary cells takes place from the conduction regime:

$$\text{Gr}_c = \frac{1 + \frac{5}{A}}{1.25 \times 10^{-4}}. \quad (1)$$

In a window cavity, where A is very large, Equation 1 predicts the onset of secondary cells at Gr = 8,000 or Ra ≈ 5,700.

Discussion

The range of Ra expected in window cavities can be determined by one-dimensional simulation. Under the ASHRAE winter design condition, calculations (UW 1992) show that Ra ≈ 6.6×10^3 for a conventional double-glazed window (1/2-in. [12.7-mm] pane spacing) and Ra ≈ 8.3×10^3 for the same window with a soft, low-emissivity coating ($\varepsilon \approx 0.1$). Corresponding values of Ra for similar windows with argon fill gas are about 25% higher. If krypton is used in place of air with the same pane spacing and low-e coating, Ra will be higher by a factor of about 4.5. However, if the spacing is also reduced to the optimum value for krypton (about 1/3 in. [8 mm]) Ra will be reduced to 8.6×10^3 and 11.1×10^3 without and with a low-e coating, respectively.

It can be seen that windows constructed with optimum pane spacing and exposed to the ASHRAE winter design condition will operate with Ra ≈ 10^4. The critical value of Ra above which secondary cells can be expected is about 6×10^3. Therefore, a model that realistically accounts for the mechanisms of convective heat transfer in a glazing system must be able to account for secondary cells. Furthermore, previous research has demonstrated that, in the range of interest for window modeling (Ra < 1.2×10^4), it is not necessary to model turbulence.

TWO-DIMENSIONAL NUMERICAL MODEL FOR NATURAL CONVECTION

Formulation

The physical balances present in the laminar two-dimensional fill gas flow can be described mathematically by assuming that the fluid is Newtonian, that compressibility effects and viscous dissipation can be neglected, and that fluid properties can be taken as constant except in the formulation of the buoyancy term. The differential equations describing the conservation of energy, horizontal and vertical momentum, and mass, respectively, at any point in the flow, are

$$\rho C_p \left\{ \frac{\partial T}{\partial t} + u\frac{\partial T}{\partial x} + v\frac{\partial T}{\partial y} \right\} = k \left\{ \frac{\partial^2 T}{\partial x^2} + \frac{\partial^2 T}{\partial y^2} \right\} + S, \quad (2)$$

$$\rho \left\{ \frac{\partial u}{\partial t} + u\frac{\partial u}{\partial x} + v\frac{\partial u}{\partial y} \right\} = \mu \left\{ \frac{\partial^2 u}{\partial x^2} + \frac{\partial^2 u}{\partial y^2} \right\} - \frac{\partial P}{\partial x}, \quad (3)$$

$$\rho \left\{ \frac{\partial v}{\partial t} + u\frac{\partial v}{\partial x} + v\frac{\partial v}{\partial y} \right\} = \mu \left\{ \frac{\partial^2 v}{\partial x^2} + \frac{\partial^2 v}{\partial y^2} \right\} - \frac{\partial P}{\partial y} + \rho g \beta (T - T_m), \quad (4)$$

and

$$\frac{\partial u}{\partial x} + \frac{\partial v}{\partial y} = 0. \quad (5)$$

These coupled equations are elliptical in both the x and y dimensions. The boundary conditions are as shown in Figure 1:

$$T = T_c \quad \text{at} \quad x = 0, \quad (6)$$

$$T = T_h \quad \text{at} \quad x = \ell_x, \quad (7)$$

$$\frac{\partial T}{\partial y} = 0 \quad \text{at } y = 0 \text{ and } y = \ell_y \text{ (i.e., } ZHF), \quad (8)$$

and

$$u = v = 0 \text{ at } y = 0,\ y = \ell_y,\ x = 0, \text{ and } x = \ell_x. \quad (9)$$

A model has been formulated in order to simulate the problem shown in Figure 1. The analysis provides a numerical solution to the discretized versions of Equations 2 through 5 applied in their integral form over the boundaries of each control volume in an array of rectangular finite control volumes covering the problem domain.

The expected presence of secondary cells precludes the use of a nonuniform grid. Interesting detail can be expected everywhere in the flow, so the solution algorithm divides the problem domain using uniform grid spacings in both the x and y directions. Figure 3 shows the staggered grid formulation that has been implemented (Harlow and Welch 1965). Note that the x-direction index, i, begins at $i = ib$ and ends at $i = ie$. Similarly, the y-direction index runs from $j = jb$ to $j = je$.

The formulation of the discretized equations is conservative, with the time-dependent terms retained in order to apply the method of the "false transient" to arrive at a steady-state solution. The algorithm used to solve the four sets of coupled equations, called SIMPLEC (Vandoormaal and Raithby 1984), is an extension of the semi-implicit method for pressure-linked equations (SIMPLE) described in detail by Patankar (1980). An alternating direction implicit (ADI) solver has been employed to solve each individual set of equations.

The numerical model uses either the central difference scheme (CDS) or an upwind difference scheme (UDS) to calculate the convective and diffusive fluxes of energy and momentum at each control volume face. The calculation of T, u, or v (or their derivatives) is simplified by the use of a uniform grid. The value and spatial gradient of an entity,

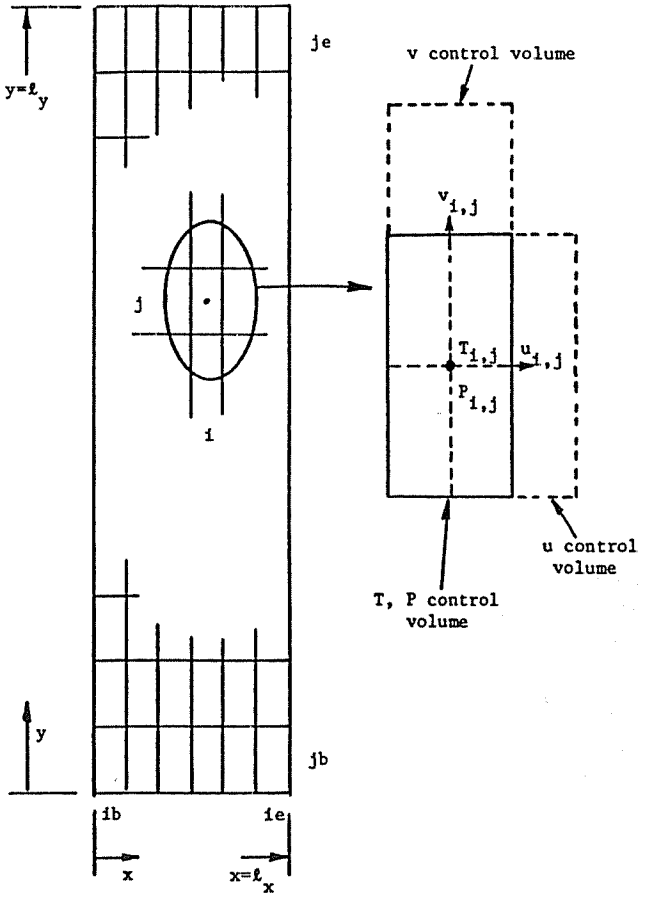

Figure 3 *The uniform, staggered grid.*

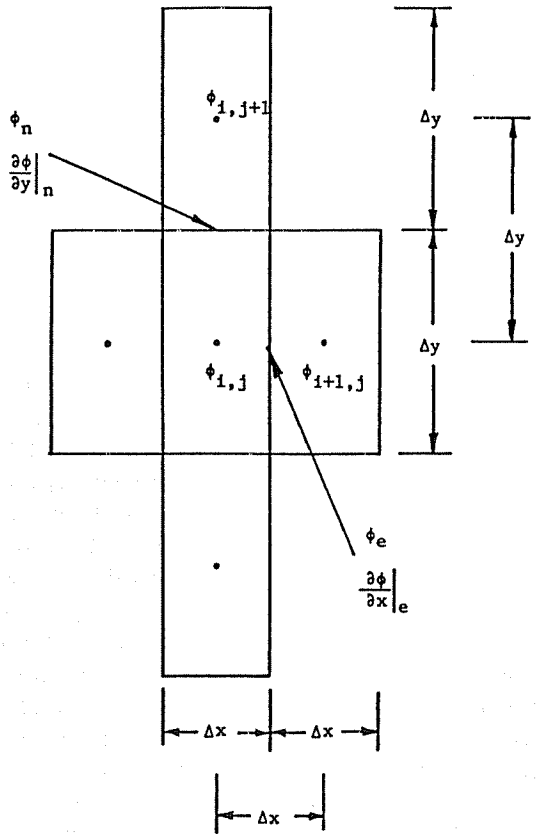

Figure 4 *Calculation of fluxes at faces in the finite-volume computational molecule.*

say, ϕ (ϕ can be T, u, or v, depending on whether flux of energy, x-momentum, or y-momentum is being examined), at the east face of a control volume is calculated as shown in Equations 10 and 11. The related geometry and nomenclature are shown in Figure 4.

$$\phi_e = \left(\frac{1}{2} + \alpha\right)\phi_{ij} + \left(\frac{1}{2} - \alpha\right)\phi_{i+1,j} \tag{10}$$

$$\frac{\partial \phi}{\partial x}\Big|_e = \frac{\beta(\phi_{i+1,j} - \phi_{i,j})}{\Delta x} \tag{11}$$

Various relations (yielding results of comparable accuracy) are available for calculating α and β. The following power law upwinding scheme (Raithby et al. 1986) has been chosen to calculate α and β as a function of the grid Peclet number, Pe:

$$\alpha = \frac{\mathrm{Pe}^2}{10 + 2\,\mathrm{Pe}^2} \tag{12}$$

and

$$\beta = \frac{1 + 0.005\,\mathrm{Pe}^2}{1 + 0.05\,\mathrm{Pe}^2} \tag{13}$$

where

$$\mathrm{Pe} = \frac{\rho\, u_{i,j}\, C_p\, \Delta x}{k}. \tag{14}$$

Similar calculations are carried out for the north control volume faces by substituting $v_{i,j}$, Δy, and $\phi_{i,j+1}$ for $u_{i,j}$, Δx, and $\phi_{i+1,j}$.

When high values of Pe occur, the flux at a control volume face is dominated by convection, so $\alpha \approx 0.5$ and $\beta \approx 0.1$. In this case, $\phi \approx \phi_{i,j}$ and $\partial\phi/\partial x$ becomes small. When Pe is small (say, Pe < 2), α and β approach 0 and 1, respectively, and the upwinding scheme, given by Equations 10 through 14, approaches the central difference scheme. The central difference scheme can be imposed manually by setting $\alpha = 0$ and $\beta = 1$.

The central difference scheme and the upwind scheme are classified as second-order accurate and first-order accurate, respectively (Patankar 1980). Some researchers who have successfully modeled secondary cells in natural convection have found it necessary to use higher order schemes (Lee and Korpela 1983; Korpela et al. 1982; Ramanan and Korpela 1989; Roux et al. 1979). For example, Lee and Korpela's (1983) model incorporates a fourth-order scheme that requires a 13-point computational molecule. Other models (de Vahl Davis and Jones 1984; Lauriat and Desrayaud 1985) have resolved secondary cells with CDS formulations. The numerical model used in the current study uses the CDS formulation when secondary cells are expected, and UDS is used when cells are not expected.

The current model differs from SIMPLEC only in that the additive correction method (ACM) presented by Hutchinson and Raithby (1986) has been used to accelerate convergence when solving the pressure correction (*P*-prime) portion of the SIMPLEC procedure. The ACM algorithm is a multigrid method that is useful when individual control volumes are oblong. The control volumes must be much taller than they are wide in the analysis of the vertical slot in order to limit computer storage and run time. The ACM applies additive pressure corrections to blocks of control volumes by solving the *P*-prime set of equations for a course grid where each control volume consists of a single horizontal row of control volumes from the finer grid. The control volumes in the course grid are also oblong but their orientation is horizontal rather than vertical, allowing for pressure correction information to be moved more rapidly in the vertical direction.

The ACM method does not alter the formulation of the governing equation nor does it alter its solution. It is used solely to speed the convergence of the iterative solver. Detailed information can found in references by Ramanan and Korpela (1989) and Hutchinson and Raithby (1986).

Grid Sizing

Throughout the current study, the grid aspect ratio has been set equal to 5 (i.e., $A_{grid} = (\Delta y/\Delta x) = 5$) as a compromise to limit computer requirements while avoiding an extreme imbalance in the areas of the vertical and horizontal faces of the finite control volumes. In their studies, Raithby and Wong (1981) used less than 2,000 grid points at $A = 40$ (12 × 160) and Lee and Korpela (1983) used slightly more than 2,000 (17 × 129) at $A = 20$. Ramanan and Korpela (1989) used a 32 × 256 grid ($A > 17.5$), Korpela et al. (1982) used a 17 × 65 grid ($10 < A < 20$), and de Vahl Davis and Jones (1984) used an 11 × 41 grid ($A = 20$). Grid aspect ratios used in these studies ranged from 2.5 to 5.4. Lauriat and Desrayaud (1985) set the number of vertical divisions equal to 10 times the aspect ratio and used up to 31 horizontal divisions ($10 < A < 20$).

In order to test for grid dependence in the calculated results, simulations were completed with $A = 40$ and Ra = 8,239. The computed Nusselt number, Nu (i.e., total heat transfer over the height of the cavity), did not differ in the third significant digit between the 25 × 200 and 30 × 240 grids. Nu changed by about 1% when the grid was reduced to 20 × 160. Secondary cells were expected ($Ra_c = 6{,}413$), and 15 cells were modeled in each of the three simulations. All subsequent runs were carried out using 25 horizontal divisions.

Perturbation

Two previous studies have been mentioned where secondary cells were modeled using the CDS formulation. Cells were reported only for Ra as low as 20,000 in one case (de Vahl Davis and Jones 1984) and as low as about 22,000 in the other case (Lauriat and Desrayaud 1985). Both simulations used $A = 20$, so secondary cells might have been expected for Ra > 7,150 (see Equation 1). In the present study, cells arose naturally from the numerical simulation at Ra = 16,479 and $A = 40$ using the CDS formulation. However, knowing that two or more solutions might exist at a still lower Ra, it was thought that the simulation might select a solution with secondary cells if it were given a "push." It has been discovered that secondary cells can be modeled with Ra approaching the theoretical critical value by perturbing the flow.

The procedure used to generate secondary cells consists of several steps. First, the solution for a unicellular base flow is established using the upwind scheme. This can be done using relatively large time steps, say, 50 times as great as the maximum time step possible for stability in an explicit formulation. Second, the solution scheme is switched to CDS and the time step is reduced to the maximum explicit time step. Third, cells are introduced by summing the existing velocity field with a "perturbation" velocity field that resembles secondary cells alone. Finally, the SIMPLEC iteration process is allowed to continue to convergence. This stepwise procedure provides a useful way to directly examine the differences that secondary cells create.

The velocity perturbation field was formulated on the basis of information given by Lee and Korpela (1983). The height of a single secondary cell, ℓ_c (or the distance between the centers of adjacent cells), can be expressed in terms of a wave number, α_c, according to Equation 15:

$$\ell_c = \left(\frac{2\pi}{\alpha_c}\right)\ell_x . \tag{15}$$

α_c was calculated as a function of Gr by interpolating between the wave numbers observed in the simulation results reported by Lee and Korpela (1983). These are

$$\alpha_c = 2.82 \quad \text{at} \quad Gr = 11{,}000$$
$$\alpha_c = 2.50 \quad \text{at} \quad Gr = 15{,}000$$

$$\alpha_c = 2.41 \quad \text{at} \quad Gr = 20{,}000$$
$$\alpha_c = 2.33 \quad \text{at} \quad Gr = 25{,}000.$$

These data show that the secondary cells lengthen as Gr (or Ra) is increased. The theoretical wave number expected for cells at $Ra = Ra_c$ and $A \rightarrow \infty$ is $\alpha_c = 2.8$ (Bergholz 1978). When Gr was less than 11,000, α_c was set equal to 2.82. The number of cells, n_c, is calculated using Equation 16, which is also based on data presented by Lee and Korpela (1983):

$$n_c = \text{int}\left[\frac{A - 10}{(2\pi/\alpha_c)}\right] + 2. \tag{16}$$

Once the number and size of secondary cells had been determined, the perturbation velocity components, u_c and v_c, were calculated in terms of the perturbation stream function, Ψ_c, according to the convention:

$$u_c = -\frac{\partial \Psi_c}{\partial y} \tag{17}$$

and

$$v_c = \frac{\partial \Psi_c}{\partial x}. \tag{18}$$

The perturbation stream function used for all simulations is given by the following equations:

$$\Psi_c = X(x) \cdot Y(y) \tag{19}$$

where

$$X(x) = \frac{1}{2} + \frac{1}{2}\cos\left(2\pi\left(\frac{x}{\ell_x} - \frac{1}{2}\right)\right) \tag{20}$$

and

$$Y(y) = -1 + \cos\left(\alpha_c A\left(\frac{y}{\ell_y} - \frac{1}{2}\right) + n_{o/e}\,\pi\right). \tag{21}$$

$n_{o/e} = 1$ if n_c is odd, and $n_{o/e} = 0$ if n_c is even.

Equation 20 applies over the following range:

$$\frac{\ell_y - n_c \ell_c}{2} < y < \frac{\ell_y + n_c \ell_c}{2}.$$

Otherwise, near the ends of the cavity,

$$Y(y) = 0. \tag{22}$$

The components of the perturbation velocity, u_c and v_c, conserve mass by virtue of their stream function formulation. The stream function, Ψ_c, has been chosen so that u_c and v_c also comply with the zero-slip boundary condition set out in Equation 9.

The perturbation, Ψ_c, was applied over the solution grid and scaled such that the maximum value of u_c would be equal to the maximum value of u known to exist in the unicellular base flow, u_{max}. Using the discretized counterparts of Equations 17 and 18, the perturbation velocity components at the east and north faces of any control volume, u_c and v_c, respectively, are

$$u_c = \frac{2u_{max}(\Psi^{se} - \Psi^{ne}) \cdot (je - jb + 1)}{\alpha_c A} \tag{23}$$

and

$$v_c = \frac{2u_{max}(\Psi^{ne} - \Psi^{nw}) \cdot (ie - ib + 1)}{\alpha_c}. \tag{24}$$

The variables Ψ^{se}, Ψ^{ne}, and Ψ^{nw} represent Ψ_c evaluated at the southeast, northeast, and northwest corners, respectively, of the control volume.

Solution Procedure

In order to arrive at a numerical solution, the procedure marches through time using the distorted transient formulation. The cycle of formulating coefficients and solving for each of T, u, v, and the P-prime (P') pressure correction corresponds directly to the SIMPLEC algorithm. This cycle is called the coefficient update loop. The numerical solution of each of these variables was carried out using an ADI solver, and ACM block correction was applied to speed the solution for P'.

The ADI solver is used to solve for a set of simultaneous equations of the form shown in Equation 25. Given a set of a and b coefficients for each control volume, the solver returns the solution for $\phi_{i,j}$:

$$a_p \phi_{i,j} = a_e \phi_{i+1,j} + a_w \phi_{i-1,j} + a_n \phi_{i,j+1} + a_s \phi_{i,j-1} + b_p. \tag{25}$$

Operation of the ADI solver was terminated either when it had executed a specified maximum number of passes over the problem domain or when it had solved $\phi_{i,j}$ to within a specified tolerance. The degree of solution convergence was determined by calculating the residual in the ϕ solution (R_ϕ) given by the root-mean-square (RMS) average of the residuals at each control volume ($R_{i,j}$) in the problem domain. $R_{i,j}$ is the difference between the two sides of Equation 25:

$$R_{i,j} = a_e \phi_{i+1,j} + a_w \phi_{i-1,j} + a_n \phi_{i,j+1} + a_s \phi_{i,j-1} + b_p - a_p \phi_{i,j}. \tag{26}$$

The ideal goal in executing the solver is to reduce all $R_{i,j}$ to zero. The ADI solver was terminated if R_ϕ was reduced by a factor of 10^4. Otherwise, the number of ADI double-

passes was limited to about eight, four, and five while solving for T, u, and v, respectively. The P' solution was allowed to run for seven iterations following the application of ACM block correction. The combination of ACM correction plus seven ADI iterations was repeated as many as seven times, making for a possible total of 49 ADI iterations in solving for P'.

The desired residual reduction factor of 10^4 was readily reached for all variables early in the solution procedure, with the P' solution (which always requires the majority of the CPU time) usually needing only 14 ADI passes. During coefficient loop passes late in the solution procedure, there was little improvement to be made in the values of T, u, v, and P', so a smaller amount of residual reduction was available. Generally, the residual reduction was between 10^3 and 10^2 for all variables, with P' taking 49 ADI passes, by the time convergence at the level of the coefficient loop was achieved.

The P' residual can be interpreted as the RMS average mass divergence (i.e., average amount of mass generated per control volume). The application of the P' solution in correcting the flow field consistently reduced the average mass divergence to about 0.5×10^{-11} kg/s. This corresponds to an average error in velocity at control volume faces of approximately 7×10^{-10} m/s.

Convergence of the coefficient loop was determined by examining the rate of heat transfer (or Nusselt number) across various vertical planes in the vertical cavity.

Calculation of Nusselt Number

After a solution is found for the temperature and velocity fields, the heat transfer can be quantified. It is customary to express the rate of heat transfer across the cavity in terms of a Nusselt number.

Since the top and bottom surfaces of the problem domain are adiabatic, the heat transfer through any two vertical planes within the cavity must be equal. The Nusselt number, Nu, based on the average horizontal heat flux from the hot wall to the cold wall can be calculated by summing the conductive and convective components of heat transfer from the bottom to the top of any vertical cut:

$$\mathrm{Nu} = \frac{1}{q_o} \int_{y=0}^{\ell_y} \left(k \frac{\partial T}{\partial x} - \rho C_p u (T - T_{ref}) \right) dy \qquad (27)$$

where

T_{ref} = constant reference temperature and
q_o = reference heat flux used to render Nu dimensionless and is chosen, consistent with convention, to be the heat flux expected if the gas layer were stagnant:

$$q_o = \frac{k}{\ell_x} (T_h - T_c). \qquad (28)$$

Equation 27 can be simplified by splitting the convection term into two parts and noting that the net amount of mass crossing any vertical plane must be zero:

$$\int_{y=0}^{\ell_y} \rho C_p u T_{ref} \, dy = C_p T_{ref} \int_{y=0}^{\ell_y} \rho u dy = 0. \qquad (29)$$

Thus, it is unnecessary to specify a value for T_{ref} in order to calculate Nu:

$$\mathrm{Nu} = \frac{1}{q_o} \int_{y=0}^{\ell_y} \left(k \frac{\partial T}{\partial x} - \rho C_p u T \right) dy. \qquad (30)$$

The local Nusselt number, Nu(y), can be evaluated at either wall where $u = v = 0$:

$$\mathrm{Nu}(y) = \frac{k}{q_o} \frac{\partial T}{\partial x} \quad (\text{at } x = 0 \text{ or } x = e_x). \qquad (31)$$

It is apparent, because of the symmetry that exists, that Nu(y) at either of the vertical walls is equal to Nu($e_y - y$) at the opposite wall.

The discretized versions of Equations 30 and 31 have been used to calculate Nusselt numbers for the numerical simulation. It can be shown that Nu, calculated at a vertical plane running coincident with the right-hand side of the ith column of control volumes, is given by

$$\mathrm{Nu} = \frac{n_x}{n_y (T_h - T_c)} \sum_{j=jb}^{je} \left\{ \beta (T_{i+1,j} - T_{i,j}) - \mathrm{Pe} \left[\left(\frac{1}{2} + \alpha \right) T_{i,j} + \left(\frac{1}{2} - \alpha \right) T_{i+1,j} \right] \right\} \qquad (32)$$

where

n_x = $ie - ib + 1$ = number of columns of control volumes and
n_y = $je - jb + 1$ = number of rows of control volumes.

The local values of α, β, and Pe are given by Equations 12 through 14 if UDS is being used or $\alpha = 0$ and $\beta = 1$ if CDS is being used.

The value of Nu at the hot vertical wall (where $u = 0$, so $\mathrm{Pe} = \alpha = 0$ and $\beta = 1$) is

$$\mathrm{Nu} = \frac{2 n_x}{n_y} \sum_{j=jb}^{je} \frac{T_h - T_{ie,j}}{T_h - T_c}. \qquad (33)$$

The local Nusselt number at the hot wall is simply

$$\mathrm{Nu}(y) = 2 n_x \frac{T_h - T_{ie,j}}{T_h - T_c}. \qquad (34)$$

Test for Convergence of Coefficient Loop

Convergence of the solutions for T, u, and v at the coefficient loop level was tested by calculating Nu at each vertical control volume division. The problem domain was divided horizontally into 25 columns of control volumes so that it was possible to calculate Nu by applying Equation 32 in 26 different places. While making these calculations, the maximum, minimum, and average values of the calculated Nusselt numbers, Nu_{max}, Nu_{min}, and Nu_{avg}, respectively, were noted.

The level of convergence was tested by calculating the percent difference between Nu_{max} and Nu_{min}, denoted $\Delta Nu_{\%}$:

$$\Delta Nu_{\%} = \frac{Nu_{max} - Nu_{min}}{Nu_{avg}} \times 100\% .$$

Simulations were run well beyond the number of iterations required for Nu_{max} and Nu_{min} to be equal and to remain unchanged in the third significant decimal place. Generally, these conditions were met if $\Delta Nu_{\%}$ was reduced to (or near) 0.1%.

The condition of $\Delta Nu_{\%} < 0.1\%$ could not be used as the sole criterion for convergence. When simulations were performed at higher values of Ra (Ra = 13,732 and 16,479 at $A = 40$), $\Delta Nu_{\%}$ fell below 0.1% within 100 iterations of the coefficient loop following the perturbation of secondary cells but rose and fell again in a decaying cyclic fashion; after about 400 iterations it finally took on a steady cyclic pattern but always remained below 0.5%. Similar difficulties in obtaining convergence were noted by Raithby and Wong (1981). In order to guard against early termination, the program was run for a fixed number of iterations and the results were examined manually. In cases where more iterations were required, it was possible to restart the simulation where it had left off.

Results

In order to test the numerical model, Nusselt number results were compared against two sets of measured results. One set of measurements was made by ElSherbiny (1980) using a guarded heater plate apparatus (ElSherbiny et al. 1982), and the other set was made by Shewen (1986) using a similar apparatus that makes use of the Peltier effect to measure heat transfer (Shewen et al. 1989). Simulations were performed with Ra as high as 16,479. The aspect ratio was fixed at $A = 40$. This was the value of A for which results were included in both sets of experimental data and for which other simulation results were available.

Figure 5 shows Nu plotted as a function of Ra and includes the simulation results of Raithby and Wong (1981), Lee and Korpela (1983), the present study (with and without cells), plus measured values of Nu from ElSherbiny et al. (1982) and Shewen (1986). A mix of LTP and ZHF results is shown in Figure 5. Note that Lauriat and Desrayaud (1985) pointed out, on the basis of their own investigation, that the influence of LTP or ZHF boundary conditions (on Nu) is small for $A > 10$. The measured results are marked by a band indicating the reported uncertainty levels. The straight lines connecting pairs of simulation data are intended to distinguish between sets of data and are not included as a suggested functional dependence. The simulation results from the present study are also listed in Table 1.

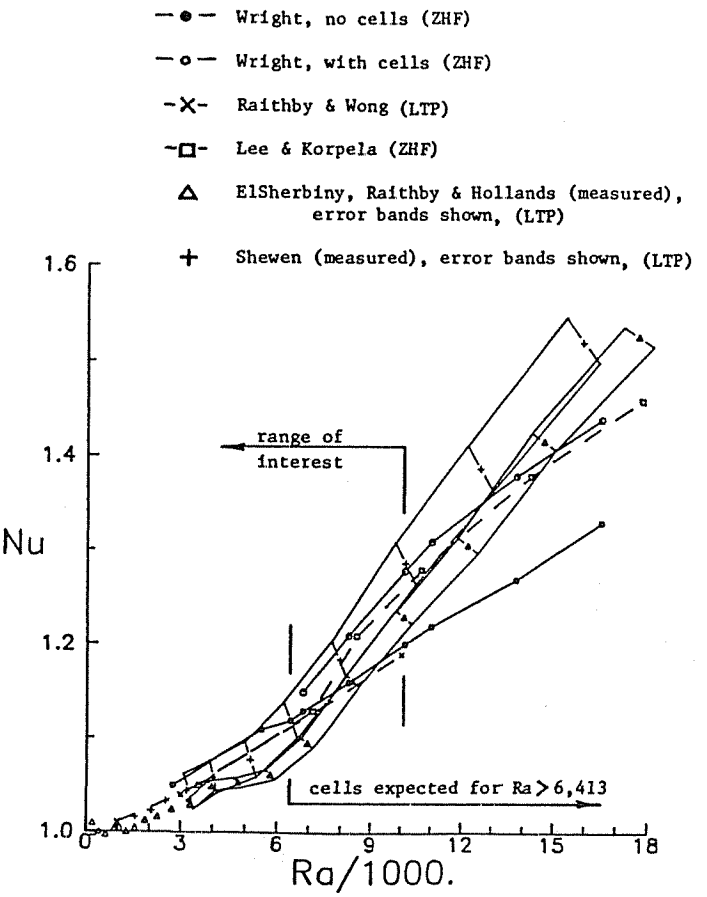

Figure 5 *Comparison of available simulation and measured Nu vs. Ra results for the vertical cavity,* A = *40.*

Several observations can be made regarding the data shown in Figure 5. The measured data of ElSherbiny et al. (1982) show the same trend as the measured data of Shewen (1986), but the Nu values given by Shewen are consistently about 4% higher than the data of Elsherbiny et al. The reason for this discrepancy is not apparent. Shewen points out that the data of ElSherbiny et al. for $A = 40$ were not consistent with the data from the same source for $A = 80$ and $A = 110$. The data for $A = 40$ depart from the Nu = 1 condition at a higher critical Rayleigh number than expected, suggesting that the $A = 40$ data of ElSherbiny may be slightly low.

TABLE 1
Nu vs. Ra Simulation Results, *A* = 40

Run #	Ra	Cells Perturbed	Cells Kept	Nu without cells	Nu with cells
1	2,746	-	-	1.05	-
2	5,493	-	-	1.11	-
3	6,413	-	-	1.12	-
5	6,800	15	15	1.13	1.15
7	8,239	15	15	1.16	1.21
9	10,102	14	14	1.20	1.28
11	10,986	13	13	1.22	1.31
13	13,732	13	13	1.27	1.38
15	16,479	13	11	1.33	1.44

Values of Nu calculated *without* perturbation of secondary cells agree with the simulation of Raithby and Wong (1981) to within about 1%. These two sets of calculated results follow the same trend that moves progressively farther from the measured data for Ra > Ra_c (Ra_c = 6,413, according to Equation 1), where the onset of secondary cells is expected. At Ra ≈ 10,000, the value of Nu for flows without cells is about 6% and 10% lower than the data of Elsherbiny et al. and Shewen, respectively. The calculated Nu data agree with the measured data of Shewen to within about 1% and to within 5% or less with the measured data of ElSherbiny et al. for Ra < Ra_c.

Values of Nu calculated *with* cells follow closely the results of Lee and Korpela (1983) (also with cells), with the discrepancy being 2% or less. In the range of Ra_c < Ra < 10,000, both of these sets of simulation results closely follow the measured data of Shewen. At Ra > 10,000, both sets of results begin to depart from the trend of the measured data. However, the calculated value of Nu does not fall below the measured data of ElSherbiny et al. until about Ra = 14,000. Clearly, the simulation is not fully modeling all of the physical mechanisms of heat transfer for Ra > 10,000. Fortunately, the range of Ra of interest for the simulation of glazing systems does not extend appreciably beyond Ra = 10,000.

In addition to reporting Nu, ElSherbiny (1980) and Shewen (1986) provide measured average values of the Nusselt number for each of the metering areas over which heat transfer was measured. ElSherbiny measured heat transfer over three heater plates, and Shewen measured heat transfer over five equal areas from the bottom to the top of the warm wall of the cavity. In order to make more detailed comparisons between calculation and measurement, the corresponding average values of the Nusselt number were calculated from simulation results by integrating Nu(y) along the hot wall within the appropriate limits of y.

The two sets of measured heat transfer results include data for almost equal values of Ra twice within the range of interest. Data were measured by ElSherbiny at Ra = 6,936 and 10,072, and Shewen presented data for Ra = 6,410 and 10,120. Two special simulation runs were executed to examine local heat transfer rates at Ra = 6,800 and 10,100. The results of these simulations are shown, in a variety of forms, in Figures 6, 7, and 8.

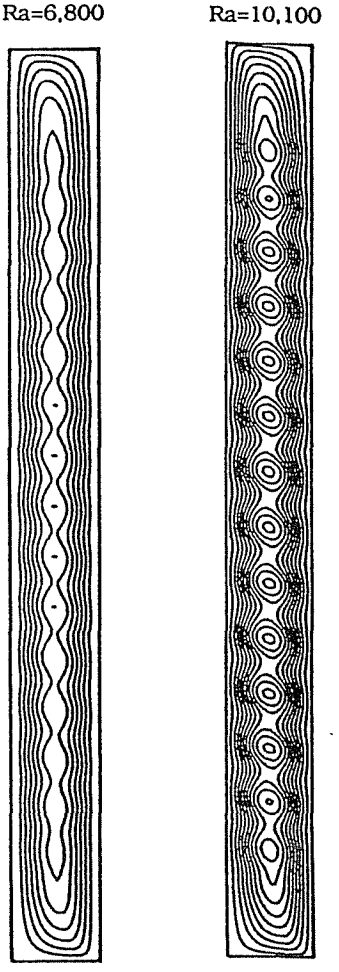

Figure 6 *Stream function plots at Ra = 6,800 and Ra = 10,100.*

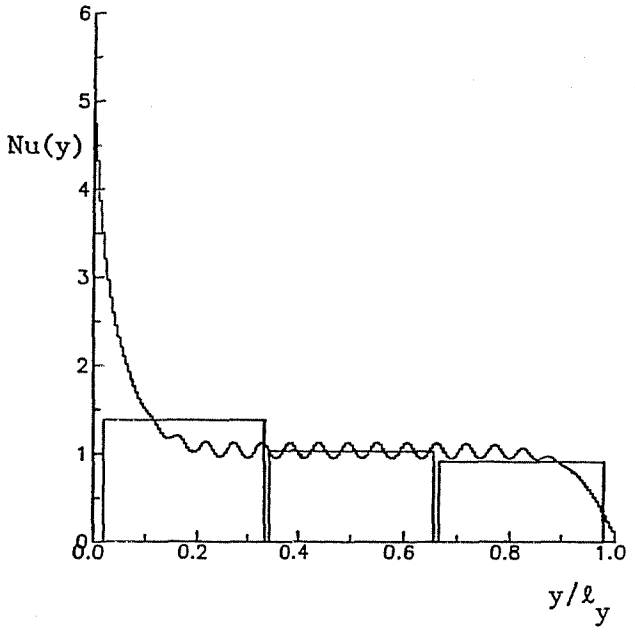

Figure 7 *Nu*(y) *vs.* y *and averaged over metering areas of ElSherbiny (Ra = 6,800,* A = *40).*

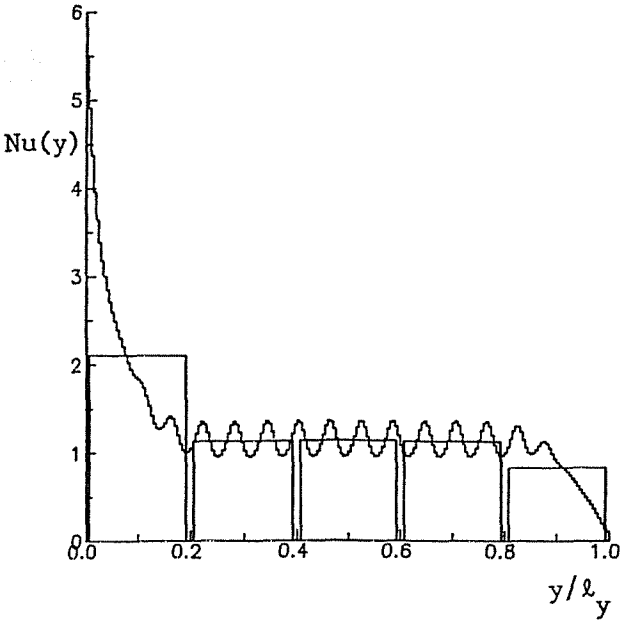

Figure 8 *Nu*(y) *vs.* y *and averaged over metering areas of Shewen (Ra = 10,100,* A = *40).*

Figure 6 shows stream function plots generated by computer simulation for Ra = 6,800 and 10,100. In each case, secondary cells were generated—15 cells at Ra = 6,800 and 14 cells at Ra = 10,100. Note that the horizontal scale has been expanded to show the detail in the flow.

Figure 7 shows the calculated Nu(y) vs. y at $x = \ell_x$ and for Ra = 6,800. Also shown are the average values of the Nusselt number calculated for the three areas corresponding to the measurement areas of ElSherbiny. Similar results are shown in Figure 8 for Ra = 10,100, but in this case, the locally averaged Nusselt numbers correspond to the five measurement areas of Shewen. Both plots of Nu(y) include wiggles that coincide with the location of the secondary cells shown in Figure 6. Comparisons between the calculated meter-area Nusselt numbers and the data of ElSherbiny and Shewen are shown in Tables 2 and 3. In order to be complete, results were also generated using the LTP boundary condition (for this comparison only) and are included in Tables 2 and 3. Little difference can be found between the LTP and ZHF results. Agreement between calculation and measurement was excellent.

Color fringe plots of T, u, and v at the bottom end of the cavity for Ra = 6,800 and Ra = 10,100 can be found in (Wright 1990).

TABLE 2
Meter-Area Nusselt Numbers—Calculation vs. Measurements of ElSherbiny, *A* = 40

Meter Location	Nusselt No. ElSherbiny (Ra=6,936) LTP	Nusselt No. Calculated (Ra=6,800) ZHF/LTP	Difference (%)	Nusselt No. ElSherbiny (Ra=10,072) LTP	Nusselt No. Calculated (Ra=10,100) ZHF/LTP	Difference (%)
Top	0.92	0.92/0.92	0/0	0.97	0.99/1.00	2/3
Middle	1.03	1.03/1.02	0/1	1.16	1.14/1.14	2/2
Bottom	1.34	1.38/1.36	3/1	1.55	1.56/1.53	1/2
Average	1.10	1.15/1.12	5/2	1.23	1.28/1.25	4/2

TABLE 3
Meter-Area Nusselt Numbers—Calculation vs. Measurements of Shewen, $A = 40$

Meter Location	Nusselt No. Shewen (Ra=6,410) LTP	Nusselt No. Calculated (Ra=6,800) ZHF/LTP	Difference (%)	Nusselt No. Shewen (Ra=10,120) LTP	Nusselt No. Calculated (Ra=10,100) ZHF/LTP	Difference (%)
Top	0.81	0.79/0.79	3/3	0.84	0.84/0.85	0/1
	1.02	1.03/1.03	1/1	1.18	1.13/1.14	4/3
Middle	1.02	1.02/1.02	0/0	1.18	1.14/1.14	3/3
	1.04	1.04/1.04	0/0	1.20	1.13/1.13	6/6
Bottom	1.72	1.82/1.74	6/1	2.05	2.10/2.00	2/2
Average	1.12	1.15/1.12	3/0	1.29	1.28/1.25	1/3

CONCLUSIONS

The Nusselt number data provided by the two-dimensional finite-volume analysis of the vertical slot for $A = 40$ demonstrate an impressive capability for the detailed simulation of fill gas flow and heat transfer. Within the range of interest ($Ra < 10^4$), the average Nusselt number (Nu) was consistently calculated to within 5% agreement with measured values, where the discrepancy between the two available sets of measured data was no better than 4%. The ability to model secondary cells contributes to the accuracy achieved for $Ra > Ra_c$ and allows the Nu vs. Ra curve to follow the correct trend up to $Ra \approx 10^4$.

The simulation has also demonstrated an ability to precisely predict local Nusselt numbers for the metering areas used in the experiments of ElSherbiny and Shewen. Again, local Nusselt numbers were predicted generally to within 5% and, in most instances, to within 2%. These discrepancies are well within experimental uncertainty.

It is concluded that the two-dimensional finite-volume analysis developed and demonstrated here realistically models the important physical mechanisms present in the vertical slot problem. Analytical results can be used both quantitatively and qualitatively to better understand these mechanisms. This simulation method can readily be extended to provide a useful analysis of the fill gas cavity between the panes of a glazing system.

ACKNOWLEDGMENTS

Glazing system research at the University of Waterloo is funded by the Energy Efficiency Technology Division, CANMET, Department of Energy, Mines and Resources Canada and by the Natural Sciences and Engineering Research Council of Canada.

Appreciation is extended to Professor G.D. Raithby of the University of Waterloo for suggestions leading to the successful formulation of the natural convection perturbation scheme.

REFERENCES

ASHRAE. 1993. *1993 ASHRAE handbook—Fundamentals.* Atlanta: American Society of Heating, Refrigerating and Air-Conditioning Engineers, Inc.

Bergholz, R.F. 1978. Instability of steady natural convection in a vertical fluid layer. *Journal of Fluid Mechanics* 84(4): 743-768.

Chait, A., and S.A. Korpela. 1989. The secondary flow and its stability for natural convection in a tall vertical enclosure. *Journal of Fluid Mechanics* 200: 189-216.

de Vahl Davis, G., and I.P. Jones. 1984. The effect of vertical temperature gradients on multi-cellular flows in high aspect ratio cavities. *Proceedings of the Conference on Liquid Metal Technology in Energy Production*, Oxford, UK, pp. 9-13.

EE. 1989. FRAME: A finite difference computer program to evaluate thermal performance of window frame systems—Version 2.0. Waterloo, ON: Enermodal Engineering Ltd.

ElSherbiny, S. 1980. Heat transfer by natural convection across vertical and inclined air layers. Ph.D. thesis. Waterloo, ON: University of Waterloo, Department of Mechanical Engineering.

ElSherbiny, S.M., G.D. Raithby, and K.G.T. Hollands. 1982. Heat transfer by natural convection across vertical and inclined air layers. *Journal of Heat Transfer* 104.

Frank, T., and H. Mühlebach. 1987. Coefficient de transmission thermique des fenêtres. *Ingénieurs et Architectes Suisse.*

Fraser, R.A., P.F. de Abreu, J.L. Wright, H.F. Sullivan, and Y. Huafo. 1993. Critical issues in comparing edge-seal performance: Modeling versus experiment. *ASHRAE Transactions* 99(1): 923-938.

Harlow, F.H., and J.E. Welch. 1965. Numerical calculation of time-dependent viscous incompressible flow of fluid with free surface. *Physics of Fluids* 8: 2182.

Hutchinson, B.R., and G.D. Raithby. 1986. A multigrid method based on the additive correction strategy. *Numerical Heat Transfer* 9: 511-537.

Korpela, S.A., Y. Lee, and J.E. Drummond. 1982. Heat transfer through a double pane window. *Journal of Heat Transfer* 104: 539-544.

Lauriat, G., and G. Desrayaud. 1985. Natural convection in air-filled cavities of high aspect ratio: Discrepancies between experimental and theoretical results. *Proceedings of the National Heat Transfer Conference*, Denver, CO, August. New York: American Society of Mechanical Engineers.

Lee, Y., and S.A. Korpela. 1983. Multicellular natural convection in a vertical slot. *Journal of Fluid Mechanics* 126: 91-121.

Patankar, S.V. 1980. *Numerical heat transfer and fluid flow.* New York: Hemisphere Publishing Corp.

Raithby, G.D., and H.H. Wong. 1981. Heat transfer by natural convection across vertical air layers. *Numerical Heat Transfer* 4: 447-457.

Raithby, G.D., K.G.T. Hollands, and T. Unny. 1977. Analysis of heat transfer by natural convection across vertical fluid layers. *Journal of Heat Transfer* 99: 287-293.

Raithby, G.D., P.F. Galpin, and J.P. VanDoormaal. 1986. Prediction of heat and fluid flow in complex geometries using general orthogonal coordinates. *Numerical Heat Transfer* 9: 125-142.

Ramanan, N., and S.A. Korpela. 1989. Multigrid solution of natural convection in a vertical slot. *Numerical Heat Transfer* 15: 323-339.

Roux, B., J.-C. Grondin, and P. Bontoux. 1979. Natural convection in inclined rectangular cavities. *Proceedings of the International Conference on Numerical Methods in Thermal Problems*, Swansea, UK. Swansee, UK: Pineridge Press.

Shewen, E.C. 1986. A Peltier-effect technique for natural convection heat flux measurement applied to the rectangular open cavity. Ph.D. thesis. Waterloo, ON: Department of Mechanical Engineering, University of Waterloo.

Shewen, E.C., K.G.T. Hollands, and G.D. Raithby. 1989. The measurement of surface heat flux using the Peltier effect. *Journal of Heat Transfer* 111(3): 708-803.

UW. 1992. *VISION3 glazing system thermal analysis: User manual.* Waterloo, ON: Advanced Glazing System Laboratory, University of Waterloo.

Vandoormaal, J.P., and G.D. Raithby. 1984. Enhancements of the SIMPLE method. *Numerical Heat Transfer* 7: 147-163.

Wright, J.L. 1990. The measurement and computer simulation of heat transfer in glazing systems. Ph.D. thesis. Waterloo, ON: Mechanical Engineering Department, University of Waterloo.

Wright, J.L., and H.F. Sullivan. 1988. Glazing system u-value measurement using a guarded heater plate apparatus. *ASHRAE Transactions* 94(2).

Wright, J.L., and H.F. Sullivan. 1989a. Natural convection in sealed glazing units: A review. *ASHRAE Transactions* 95(1).

Wright, J.L., and H.F. Sullivan. 1989b. Thermal resistance measurement of glazing system edge-seals and seal materials using a guarded heater plate apparatus. *ASHRAE Transactions* 95(2).

Wright, J.L., P.F. de Abreu, R.A. Fraser, and H.F. Sullivan. 1994. Heat transfer in glazing system edge-seals: Calculations regarding various design options. *ASHRAE Transactions* 100(1).

DISCUSSION

Rhyn H. Kim, Professor, Mechanical Engineering Department, University of North Carolina, Charlotte: Would you expect a similar trend if you change the window boundaries of temperature to heat convection boundaries?

John L. Wright: I would expect the flow field to be largely unchanged, although local heat transfer rates might be affected more strongly by the changes in local wall temperature near the cavity ends.

Chris Barry, Manager of Architectural Technical Services, Libbey-Owens-Ford Co., Toledo, OH: Would the higher temperatures at the top of the cavity not reduce the gas viscosity and so cause the cells there to rotate faster thus increasing the heat transfer across the top, as compared to the bottom, of the cavity?

Wright: Studies have shown that average heat transfer rates can be predicted with fixed gas properties as long as the temperature difference is less than 10% of the absolute temperature. Also note that the viscosity and conductivity are transport properties that are closely linked (i.e., the mechanisms of momentum and heat diffusion at the molecular scale are the same). If lower viscosity causes the cells to rotate faster, the gas conductivity will also be lower. Very detailed numerical modeling could quantify the effect, but I expect that very little difference would be found.

Roger Henry, Program Manager, CANMET, Ottawa, ON, Canada: To what extent does cavity convection compared to interior side window convection contribute to condensation on the bottom of windows?

Wright: The effect of the fill gas flow is evident because condensation forms most readily at the bottom edge of the

indoor pane. The relative importance of the local effects (e.g., fill gas flow, edge-seal conduction, indoor-side convection) can best be examined by numerical modeling.

Dragan Curcija, Mechanical Engineering Department, University of Massachusetts, Amherst: Why is there a discrepancy between the computer modeling results and the experimental results at higher Rayleigh numbers?

Wright: Higher Rayleigh numbers entail increased levels of turbulence and unsteady flow. The model described here deals with neither of these phenomena.